Supplementary Information

Nanoparticle Biokinetics in Mice and Nonhuman Primates

Peter A. Chiarelli,[†,&] Richard A. Revia,[‡,&] Zachary R. Stephen,[‡,&] Kui Wang,[‡] Mike Jeon,[‡] Veronica Nelson,[§] Forrest M. Kievit,[†,‡] Jonathan Sham,[#] Richard G. Ellenbogen,[†,▽] Hans-Peter Kiem,[§,⊥] and Miqin Zhang[*,†,‡,▽]

[†]Department of Neurological Surgery, University of Washington, Seattle, Washington 98195

[‡]Department of Materials Science and Engineering, University of Washington, Seattle, Washington 98195

[§]Clinical Research Division, Fred Hutchinson Cancer Research Center, Seattle, WA 98109, USA

[#]Department of Surgery, University of Washington, Seattle, Washington 98195

[▽]Department of Radiology, University of Washington, Seattle, Washington 98195

[⊥]Department of Medicine and Pathology, University of Washington, Seattle, WA, USA.

[&]These authors contributed equally to this publication

Specific MR analytic methods for MR Data Analysis. ROIs were placed in locations that captured the largest possible area of an organ compartment. In placing ROIs, caution was taken to avoid the capsule or external margin of a given organ. Although all parenchymal ROIs inevitably contain partial volume artifact from intervening vascular structures, effort was made to avoid obvious large vessels within the selected region. Areas contaminated with vessel pulsatility artifact or respiratory artifact were avoided. The choice of common carotid artery for vascular ROI in the macaque was made, as this vessel was easily identifiable and was visualized within the slice plane for a long distance in all macaques scanned. Pulsatility artifact was not obvious for the common carotid, given the selected imaging parameters and slice orientation. The greater T2 value of the carotid vessel wall provided a good visual boundary to ensure accurate placement of the ROI. Although readily identifiable on imaging, larger vascular structures (*e.g.*, aorta, vena cava) were not chosen as vascular ROIs, due to the common aortic pulsatility artifact, which also affected the nearby vena cava. Choice of external jugular vein for vascular ROI in the mouse was made, primarily due to the large size of this vessel and lateral location in the neck. Within more central regions of the mouse neck, respiratory artifact from the trachea would intermittently overlap with the central vascular structures. Use of ear-bars for head fixation further reduced motion artifact in the head/neck, making the external jugular vein an attractive vascular choice compared to larger structures within the thorax/abdomen that could not be rigidly fixated. Given anatomy of the two species and requisite positioning in the MR coils, different regions were chosen to interrogate the signal from muscle and bone marrow. In the macaque, the shoulder and arm were contained entirely within the torso acquisition window, allowing placement of ROIs in the trapezius muscle and humeral medullary compartment; in the mouse, natural folding of the legs into the 25-mm coil for abdominal imaging made hamstring

and femur optimal choices for muscle and bone marrow ROIs, respectively. A complete list of ROI sizes is included in Table S1.

Colorized maps of signal change within the brain (Fig. 5a) were produced by digital image subtraction of co-registered T2*-W images pre- and 30 min post-IOSPM NP injection. Maps were thresholded at 10% of maximum signal change and overlaid on baseline structural images.

Data analysis to produce baseline-corrected comparative signal change plots for mouse and macaque (Fig. 5b) involved transformation of the averaged curves, with pre-injection signal arbitrarily called 0%, and max signal change during the 4 h timecourse called 100%. Although time between comparable scans for the mouse was ~10 min, macaque data was separated by a time delay of 30 min. Mouse data were therefore sub-sampled for this analysis, to include only the data points acquired at the same times as macaque data. The appearance of noise for mouse data is therefore artificially reduced in this representation, due to the inclusion of fewer values. Comparison was then performed by subtraction of normalized mouse values from normalized macaque values. The first data value (0%) was not included in this analysis, since it was artificially normalized to 0% for both mouse and macaque. If the max signal change occurred at the same time delay after NP injection for mouse and macaque (*e.g.*, 100% at 20 min), these data were also not included in the comparison. Inclusion of data in the comparative analysis was denoted by presence of a grey rectangle surrounding the data.

R2′ values were obtained by the equation:

$$R2' = \frac{1}{T2^*} - \frac{1}{T2} \qquad (1)$$

Interleaved quantitative T2* (QT2*) and QT2 data were obtained from the first macaque, using equivalent ROIs in the blood (common carotid artery), muscle, renal cortex, bone marrow (humerus), brain (deep grey matter) and liver.

Plasma half-life. Macaque blood samples for ICP measurement were collected at 0.5, 1, 2 and 4 h post-NP injection, and plasma was prepared by centrifugation of whole blood at 2,000×g for 15 min at 4°C. 80 µl of plasma was reacted with 120 µl 12 M hydrochloric acid (HCl) overnight at room temperature and diluted to 6 ml with deionized water (75× dilution). 3 aliquots (1 ml each) of the prepared blood plasma solutions were analyzed 3 times each by ICP-AES to determine the iron content of the samples.

Practical exploration of bulk magnetic susceptibility effects

A biophysical influence on T2 behavior arises from microscopic NP compartmentalization as it travels through the body and into cells. A number of studies have investigated the relationship between static dephasing regime (SDR) theory and the transverse relaxation parameters T2 and T2*.[1,2] Theoretical and experimental work with cells has suggested that spatially confined superparamagnetic NPs (*e.g.*, clustered in vesicles) will display altered magnetic decay properties; at close proximity the NPs begin to act as a bulk magnetic material, rather than as discrete magnetic domains.[3] The end result of clustering increases the local field inhomogeneities generated by the NPs, with the T2* parameter especially affected. *Via* this effect, the parameter T2′ has been explored for its potential proportionality to the intracellular uptake of NPs.[4] Given our technique of interleaved QT2 and QT2* imaging, we were able to acquire T2* data over the full 4 h timecourse, and calculate R2′ (1/T2′) for various organ compartments (**Fig. S1**). It is prudent to consider that NP aggregation *in vivo* can be far different

from that observed in cell culture. For instance, physical clustering of NPs can occur by NP binding to extracellular matrix proteins in the interstitium, as well as albumin in the blood.[5] Furthermore, NP uptake within white or red blood cells will induce NP clustering, leading to partial volume artifacts from the enhanced T2* of blood that masquerade as uptake into cells of the target organ. Given that cellular experiments found a minimal impact of clustering on the T2 parameter,[1] and realizing the multiple factors confounding the *in vivo* interpretation of R2′, we primarily rely on QT2 trends to make qualitative assessments of NP trafficking, and inspect T2* and T2′ as supplementary points of interest.

Supplementary Figures

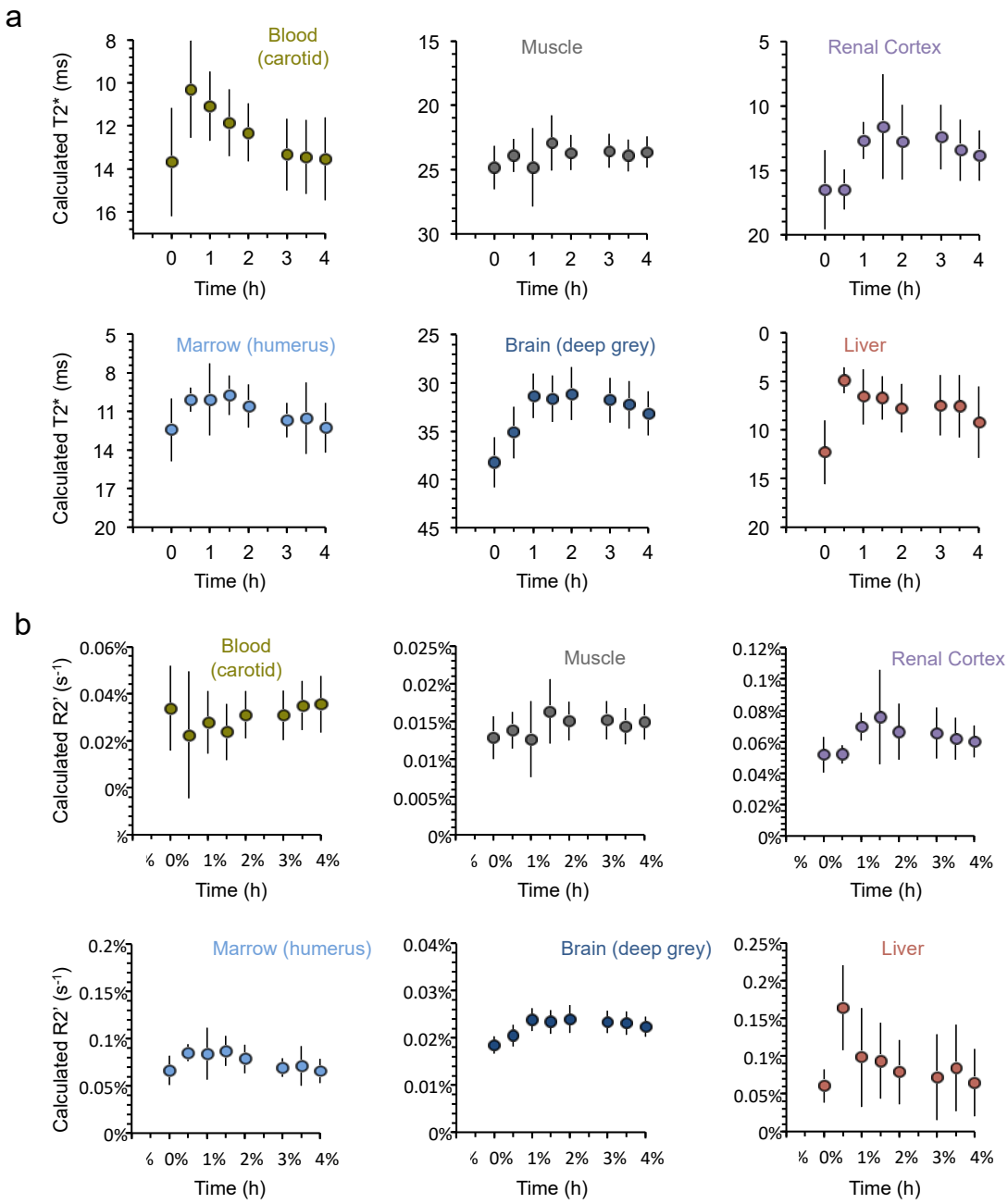

Figure S1. T2*-W and R2′ values for macaque. **a**, T2*-W values for one macaque versus time in various organs of interest. **b**, Calculated R2′ versus time in one macaque where R2′ = R2* - R2, R2 = 1/T2 and R2* = 1/T2*.

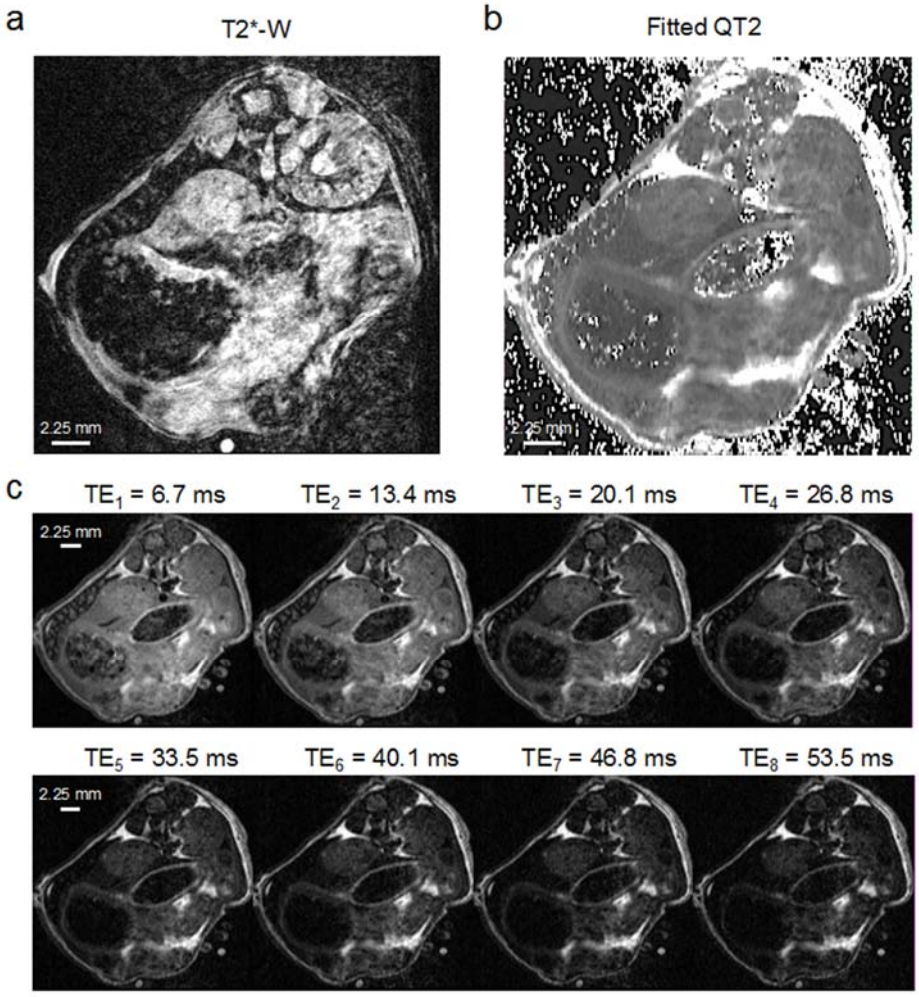

Figure S2. Representative transverse raw MR images of the mouse abdomen. **a**, T2*-W image, and **b**, QT2 map calculated by automated curve fitting. **c,** Spin-echo images obtained during scanning and used to calculate QT2 maps. The first eight raw spin echo images are shown as an example, although 16 echoes were acquired during each scan.

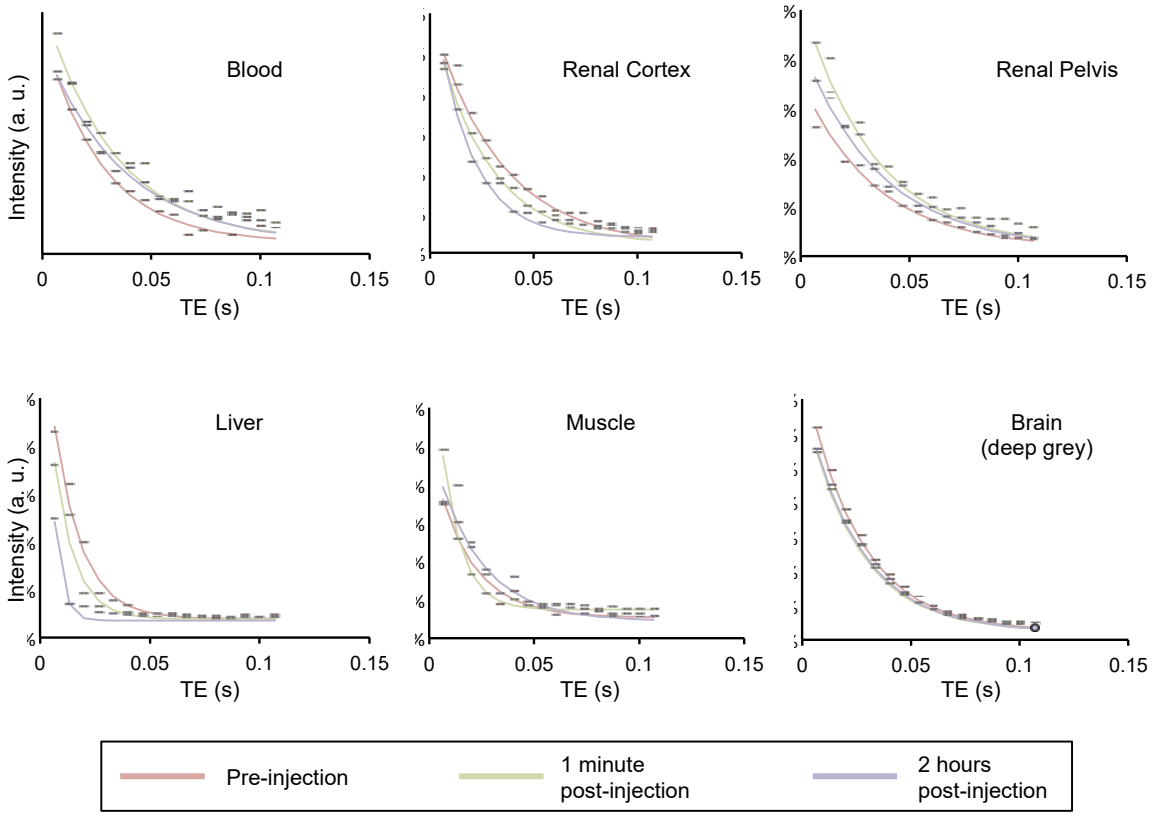

Figure S3. T2 decay profiles in multiple organs pre- and post-NP injection. Anatomical ROI-averaged signal intensity over 16 sequential spin-echoes of an MSME sequence is used for non-linear curve fitting and calculation of T2. Data points in red were obtained prior to NP injection, green data were acquired 1 min after injection, and purple data were acquired 2 h after injection. Trend lines demonstrate the accuracy of manual non-linear curve fitting, using the function $y = Ae^{(-1/T2)t}$.

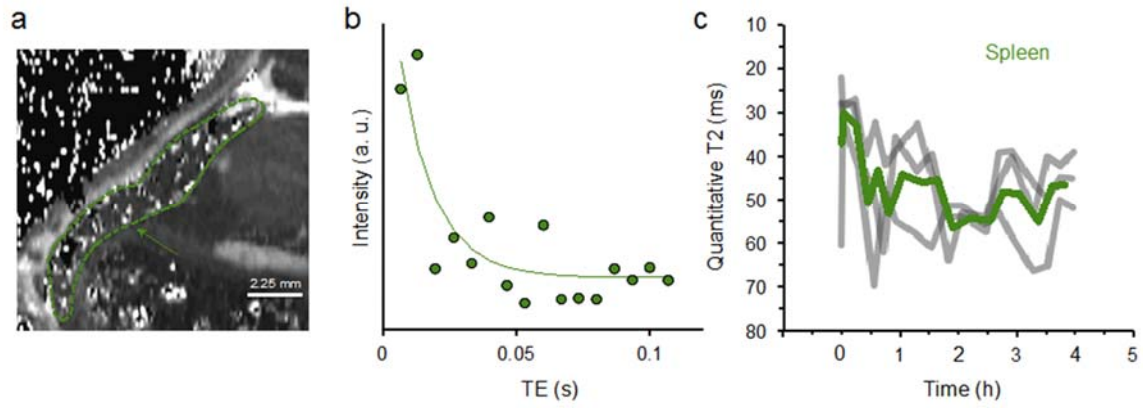

Figure S4. High variability in splenic mouse QT2 data. **a**, Fitted QT2 scan with a dashed green outline highlighting the splenic border. Numerous bright and dark voxels within the spleen represent areas of poor automated fit. **b**, Representative T2 decay curve from the spleen, with T2-weighted signal plotted over 16 sequential spin-echoes. Raw data contains high degree of noise, contributing to error in exponential curve fits. **c**, Individual QT2 timecourses in the spleens of three mice are shown in grey with the average signal superimposed in green. The variation between sequential calculated values over time is substantially greater than that seen in all other organ compartments.

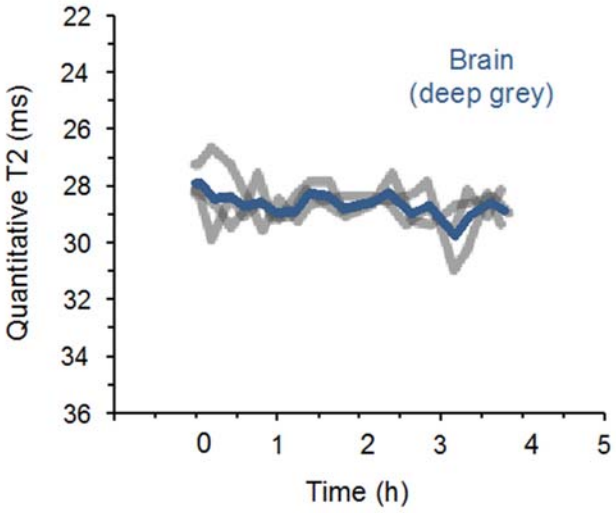

Figure S5. Calculated T2 values over time in the mouse brain. QT2 traces from the brains of individual mice are shown in grey, while the average is displayed in blue.

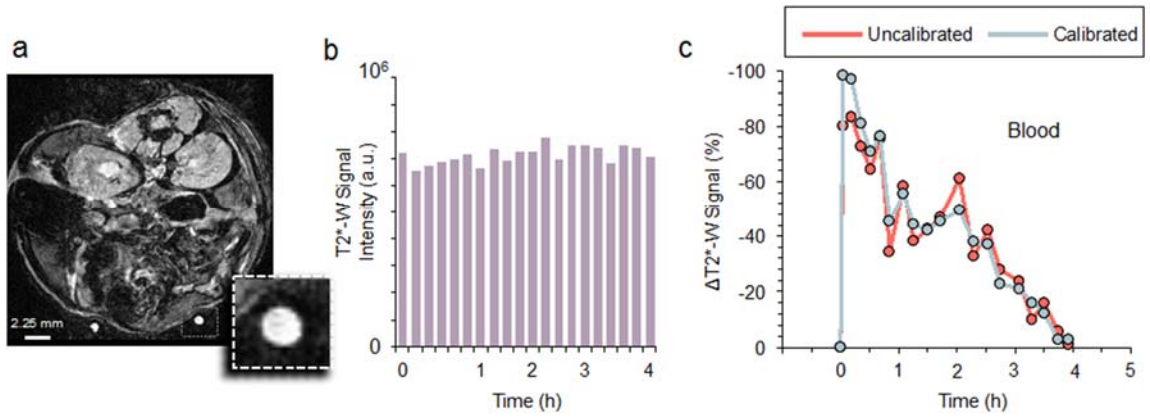

Figure S6. Water phantom calibration for T2*-weighted data. **a,** Representative T2*-W image of the mouse abdomen is shown, highlighting the location of dual water tube phantom used for signal calibration. **b**, T2*-W signal intensity averaged over the two water tubes, from each sequential scan during a 4 h timecourse. Fluctuations in T2*-W signal within the water phantom are assumed proportional to fluctuations over the entire image, and occur due to differences in automated gain settings, pulse power and sensitivity changes in scanner hardware over time. **c**, Example of the change in T2*-W timecourse provided by water phantom correction. ROI-averaged T2*-W signal in the external jugular vein prior to correction (red curve) and after correction (blue curve). Since the signal in the water tubes is relatively stable throughout the imaging timecourse, the change between the uncalibrated and calibrated trends is not dramatic; however, the uncalibrated signal does make larger departures from a linear fit than the calibrated plot indicating a reduction in noise after calibration to the water signal.

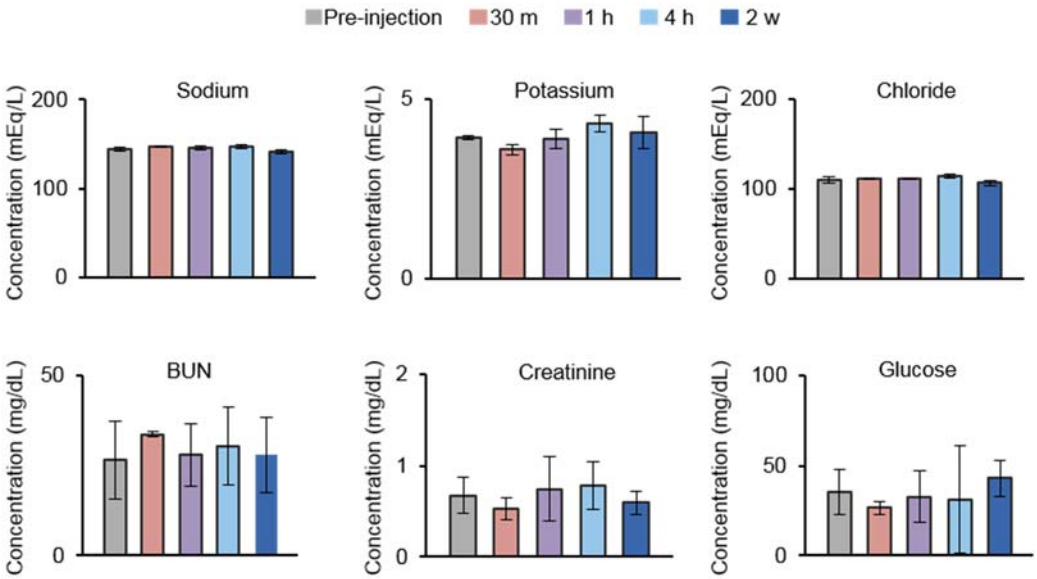

Figure S7. Macaque laboratory blood chemistry values before and after IOSPM NP injection. Electrolyte balance was maintained after IOSPM NP injection and normal levels of creatine (Cr) and blood urea nitrogen (BUN)/CR ratios were observed, indicating normal kidney function. Averages and standard deviation were determined from values from 4 macaques.

Supplementary Tables

Table S1. Average number of MRI voxels and average area included within anatomical ROIs for the macaque and mouse.

	Macaque		Mouse	
	Voxels (#)	Area (mm^2)	Voxels (#)	Area (mm^2)
Blood	34	30	15	0.3
Muscle	227	200	105	2.0
Renal cortex	170	150	98	1.9
Renal pelvis	49	43	40	0.8
Spleen	193	170	82	1.6
Marrow	41	36	58	1.1
Brain	136	120	160	3.0
Liver	170	150	340	6.4

References

1 Bowen, C. V.; Zhang, X.; Saab, G.; Gareau, P. J.; Rutt, B. K. Application of the Static Dephasing Regime Theory to Superparamagnetic Iron-Oxide Loaded Cells. *Magn. Reson. Med.* **2002**, *48*, 52-61.

2 Yablonskiy, D. A.; Haacke, E. M. Theory of NMR Signal Behavior in Magnetically Inhomogeneous Tissues: The Static Dephasing Regime. *Magn. Reson. Med.* **1994**, *32*, 749-763.

3 Simon, G. H.; Bauer, J.; Saborovski, O.; Fu, Y.; Corot, C.; Wendland, M. F.; Daldrup-Link, H. E. T1 and T2 Relaxivity of Intracellular and Extracellular USPIO at 1.5T and 3T Clinical MR Scanning. *Eur. Radiol.* **2006**, *16*, 738-745.

4 Kuhlpeter, R.; Dahnke, H.; Matuszewski, L.; Persigehl, T.; Wallbrunn, A. V.; Allkemper, T.; Heindel, W. L.; Schaeffter, T.; Bremer, C. R2 and R2* Mapping for Sensing Cell-Bound Superparamagnetic Nanoparticles: *In Vitro* and Murine *in Vivo* Testing. *Radiology* **2007**, *245*, 449-457.

5 Marchenko, Y. Y.; Nikolaev, B. P.; Shishkin, A. N.; Yakovleva, L. Y. An NMR-Relaxation Study of the Effect of Albumin on Aggregation of Magnetic iron Oxide Nanoparticles. *Colloid J.* **2013**, *75*, 185-190.